Open Archive Toulouse Archive Ouverte (OATAO)

OATAO is an open access repository that collects the work of Toulouse researchers and makes it freely available over the web where possible.

Any correspondence concerning this service should be sent to the repository administrator: staff-oatao@inp-toulouse.fr

Influence of synthesis route and composition on electrical properties of $La_{9.33+x}Si_6O_{26+3x/2}$ oxy-apatite compounds

A. Chesnaud [a,*], G. Dezanneau [a], C. Estournès [b], C. Bogicevic [a], F. Karolak [a], S. Geiger [a,c], G. Geneste [a]

[a] *Laboratoire Structure Propriétés et Modélisation des Solides, École Centrale Paris, Grande Voie des Vignes, 92295, Châtenay-Malabry Cedex, France*
[b] *CIRIMAT et Plateforme Nationale de Frittage Flash du CNRS (PNF2-MHT-UPS), Université Paul-Sabatier, 118 Route de Narbonne, 31062, Toulouse, France*
[c] *Faculté de Pharmacie, Université Paris-Sud, 5 Rue J-B Clément, 92296, Châtenay-Malabry, France*

Abstract

Oxy-apatite materials $La_{9.33+x}Si_6O_{26+3x/2}$ are thought as zirconia-substitutes in Solid Oxide Fuel Cells due to their fast ionic conduction. However, the well-known difficulties related to their densification prevent them from being used as such. This paper presents strategies to obtain oxy-apatite dense materials. First, freeze-drying has been optimized to obtain ultrafine and very homogeneous $La_{9.33+x}Si_6O_{26+3x/2}$ ($0 \leq x \leq 0.67$) nanopowders. From these powders, conventional and Spark Plasma Sintering (SPS) have been used leading to very dense samples obtained at temperatures rather lower than those previously reported. For instance, SPS has allowed to prepare fully dense and transparent ceramics from 1200 °C under 100 MPa. The microstructure and transport properties of such samples have been then evaluated as a function of sintering conditions and lanthanum content. It will be show that for lanthanum content higher than 9.60 per unit formula, the parasitic phase La_2SiO_5 appears leading to a degradation of conduction properties. We also show that grain boundaries and porosity (for conventionally-sintered materials) seem to have blocking effects on oxygen transport. The highest overall conductivity values at 700 °C, *i.e.* $\sigma_{700 °C} = 7.33.10^{-3}$ S cm^{-1}, were measured for $La_{9.33}Si_6O_{26}$ material conventionally-sintered at 1500 °C which contains bigger grains' size by comparison with $\sigma_{700 °C} = 4.77.10^{-3}$ S cm^{-1} for SPS-sintered materials at the same temperature but for few minutes. These values are associated with activation energies close to 0.83–0.91 eV, regardless of sintering condition, which are commonly encountered for anionic conductivity into such materials.

Keywords: SOFC electrolyte; Oxy-apatite; Freeze-drying; Nanopowders; Spark plasma sintering; Anionic conductivity

1. Introduction

Materials likely to present high oxide ions conduction are of a great interest for electrochemical devices like high temperature stream electrolysers, oxygen sensors, oxygen pumps, ion-permeating membranes or solid oxide fuel cells (SOFCs) [1–3]. Currently, yttria-stabilized zirconia (YSZ) is the most common material used as electrolyte for SOFC [4–6]. Nevertheless, because of its ohmic drop below 900 °C, an important operating temperature is required, usually around 1000 °C. The development of SOFC is partially hindered by such a high temperature which imposes the use of costly materials and accelerates their deterioration through operating cycles. It is therefore compulsory to reduce this temperature in order to improve the operability of SOFC. For that purpose, several options are considered such as reducing the thickness of YSZ electrolyte layers or developing new materials with better oxide ion conduction. Recently, high values of oxide ion conduction have been discovered in $RE_{9.33+x}Si_6O_{26+3x/2}$ (RE=La, Nd, Sm, Gd, Dy) materials [7–9]. The latter exhibit an hexagonal apatite structure which is built from isolated tetravalent $[SiO_4]^{4-}$ tetrahedrons with the RE^{3+} cations located into seven- and nine-coordinate cavity sites. The composition without extra oxide ions $RE_{9.33}Si_6O_{26}$ contains 6.7% of vacancies in the rare earth cation sublattice. This three-dimensional framework delimits channels running through the c-

* Corresponding author.
E-mail address: anthony.chesnaud@ecp.fr (A. Chesnaud).

axis of the structure, inside of which extra oxide anions are localized. The latter are presumed to be responsible for the high oxide ion conduction. According to the structural description, chemical formula of these compounds can better be written $RE_{9.33+x}\square_{0.67-x}(SiO_4)_6O_{2+3x/2}$. Studies have demonstrated that the bigger the ionic radius of rare-earth element RE^{3+}, the higher the formation enthalpies [10] (in absolute values), the better anionic conductivity and the lower activation energy [7]. Therefore, lanthanum silicates reveal the better characteristics in terms of thermodynamical stability and oxide ion conduction, required for the envisaged application. Their conductivities, for high lanthanum content, are better than those of YSZ below 650 °C [8,9,11,12] (4.3×10^{-3} S cm^{-1} for $La_{10}Si_6O_{27}$ compounds versus 1.1×10^{-3} S cm^{-1} at 500 °C) [7], but they are lower at higher temperatures. However, one of the main limitations of such materials resides in the difficulty to prepare dense ceramics [7–9,13]. Many efforts have thus been made to prepare dense materials, but these hardly led to totally convincing results. In fact, from powders prepared by solid state reaction, very high sintering temperatures (1600 °C or 1700 °C) either preceded by specific treatments (intermittent ball-milling [7,12,14,15] or attrition [16] processes) or not [17–19], are still necessary to obtain relative densities higher than 90%. More recently, densities of 93% and 97% for $La_{9.33}Si_6O_{26}$ were obtained from attrited-powders by hot-pressing technique applying 35 MPa at 1400 °C [16] or conventional sintering [20] at 1600 °C. In the same way, sol–gel based processes led to density values inferior to 95% after conventional sintering of attrited [21,22] and untreated [23–25] powders. Thus, difficulties related to densification set hurdles nearly impossible to overcome for their use as electrolyte (which requires flow gases' impermeableness) in SOFC devices. Here we present two strategies to go beyond this problem consisting in the use of conventional (CS) or spark plasma (SPS) sintering techniques on the basis of freeze-dried oxy-apatite powders. The present work wants to demonstrate how the combination of highly dispersed nanopowders and efficient sintering techniques lead to good results for the densification of $La_{9.33+x}Si_6O_{26+3x/2}$ ($0 \leq x \leq 0.67$) compounds. We also want to study the influence of lanthanum content on transport properties since previous results lead to somewhat contradictory results. The main contradiction concerns the fact that higher conduction is usually reported for the $La_{10}Si_6O_{27}$ composition for which a mixture of two phases has been most often reported. Indeed, the secondary phase is non-conductive so his presence would have a detrimental effect in the overall conductivity. From electrical measurements, made by impedance spectroscopy, we will discuss about transport properties of oxy-apatite dense samples taking into account micro-structure and composition.

2. Experimental

2.1. Powder synthesis

Polycrystalline $La_{9.33+x}(SiO_4)_6O_{2+3x/2}$ ($0 \leq x \leq 0.67$) series of lanthanum silicate compounds were synthesized by freeze-drying from a stoichiometric cation solution with acetic acid as modification agent. Four compositions, $x=0$ ($La_{9.33}Si_6O_{26}$),

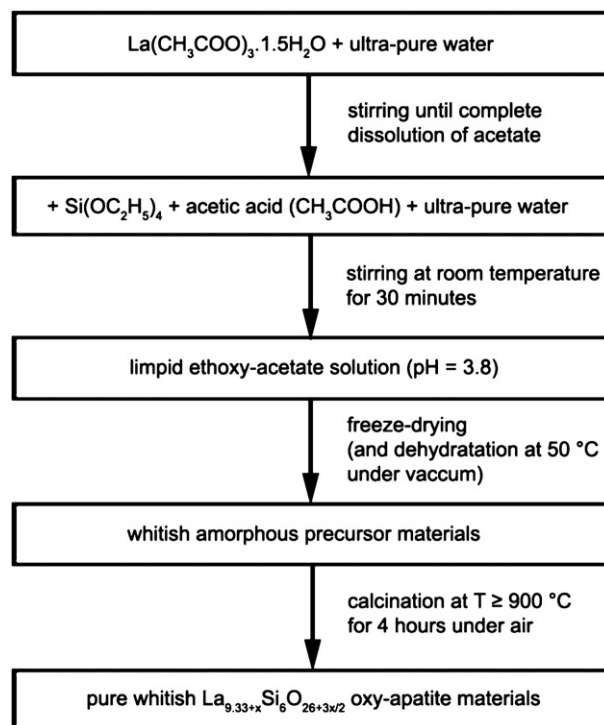Fig. 1. Flow-chart of freeze-drying for the synthesis of $La_{9.33+x}(SiO_4)_6O_{2+3x/2}$ oxy-apatite powders.

$x=0.27$ ($La_{9.60}Si_6O_{26.4}$), $x=0.47$ ($La_{9.80}Si_6O_{26.7}$) and $x=0.67$ ($La_{10}Si_6O_{27}$) were studied in this paper. To obtain ~10 g of apatite materials, a solution corresponding to a Si^{4+} cations concentration of 0.05 mol L^{-1} and total volume equal to 600 mL was prepared: based on this value, La^{3+} cations content was then calculated for each composition. Commercial reagents like lanthanum acetate sesquioxide $La(CH_3COO)_3.1.5H_2O$ (Alfa Aesar, 99.9%) and TetraEthOxySilane $Si(OC_2H_5)$ (TEOS, Strem chemicals, min. 98%) were used as La^{3+} and Si^{4+} sources, respectively. First and according to the composition, ~16–17 g of lanthanum acetate were completely dissolved into ultra-pure water. In an other beaker, a mixture containing ~6.7 mL silicium alkoxide, ~27 mL acetic acid and a small quantity of ultra-pure water was prepared and resulted into a clear transparent solution. This optimized experimental protocol [22] has been used here for the preparation of our solution. Acetic acid (AA) is a double agent used to catalyze and control the hydrolysis reaction of TEOS. For each composition, volumetric ratio $r=V_{AA}/V_{TEOS}$ has been arbitrarily fixed to 4.0. Then, the two above-mentioned solutions were mixed and no turbidity or precipitate was observed at this stage: total volume of the resulting clear transparent solution obtained was 600 mL and pH value was close to 3.8. Vigorous stirring was exerted for few minutes to assure good homogeneity. The resulting solution was sprayed into a liquid nitrogen bath to form frozen droplets in which cations stoichiometric homo-geneity was assured at the nanometric scale. Indeed, since micro-droplets were instantaneously "flash" congealed, homo-geneity of the original solution can be retained. These frozen droplets were transferred into the chamber of the freeze-dryer as

quickly as possible to prevent back-melting. The freeze-drying process was carried out in a Christ Alpha 2-4 LSC apparatus, for 24 h under vacuum (1 Pa), with the condenser's temperature fixed at −43 °C. During sublimation process, water was continuously evacuated towards the condenser, leading to a whitish porous freeze-dried precursor. As sublimation of the frozen solution occurred, the temperature of the precursor increased progressively until +10 °C. After 24 h, residual water was eliminated by increasing shelf temperature of +10 °C every hour up to +50 °C. At this stage, no variation of pressure in the chamber was recorded which means that freeze-drying was successfully achieved. The experimental procedure is summarized in the flow-chart Fig. 1. These as-prepared freeze-dried precursors were then calcinated, starting from a temperature resolved by thermogravimetric analysis to lead to the desired oxy-apatite compounds.

2.2. Sintering process conditions

In order to prepare fully dense materials using freeze-dried powders, conventional and SPS techniques have been undertaken. SPS is a powerful technique which have been employed to densify a large variety of oxides as Al_2O_3 [26], $Pb(Mg_{1/3}Nb_{2/3})_{0.7}Ti_{0.3}O_3$ [27], SnO_2 [28], TiO_2 [29,30], $BaTiO_3$ [31–33], $La_2Mo_2O_9$ [34], YSZ [35,36], CeO_2-substituted ZrO_2 [37], Sc_2O_3-substituted ZrO_2 [38] and $BaZrO_3$ [39]. It was shown that SPS allows to significantly decrease sintering temperature while operating for shorter time. It was thus tested here as an interesting alternative route to conventional sintering. For conventional sintering study, pellets were made from freeze-dried powders calcinated at 900 °C, first shaped by uniaxial pre-pressing (green densities ∼40%) in a steel die under 100 MPa and then isostatically pressed at 750 MPa for 10 min (green densities ∼65–70%). Thereafter, pellets were sintered at 1500 °C during 12 h, temperature for which a relative density higher than 95% is ensured for all compositions. SPS was performed starting from freeze-dried powders calcinated at 1000 °C for 4 h. Here, the calcination temperature of powder was slightly higher in order to avoid any residual carbon species that could not be eliminated during oxygen-free SPS. Densification was performed in a SPS Dr Sinter 2080 furnace (Sumitomo coal mining). 300–400 mg of oxy-apatite powders were directly put into a cylindrical graphite die in order to form final pellets of 8 mm in diameter and 1 mm of thickness. The die/powder assembly was then introduced into the sintering chamber. For the 1200 °C sintering, the temperature is progressively increased still its maximum while a constant pressure of 100 MPa was applied. Temperature and pressure were maintained during 3 min and then they were released. For the 1500 °C sintering temperature, the 100 MPa pressure and the power are released when the desired temperature is reached. Natural cooling of the system takes then around 10 min. At this point, all samples were subjected to heat-treatment at 1000 °C for 1 h to burn all residual carbonaceous species deposited throughout them and arising from the graphite die pressure. This last step has not been optimized and can probably be shortened in time and lowered in temperature. For our studies, relative densities of sintered-bodies were calculated from the dimensions and weight of each sample.

2.3. Physico-chemical characterisations

Simultaneous thermogravimetric (TG) and differential scanning calorimetry (DSC) analyses were performed on a small quantity (∼13 mg) of freeze-dried precursor. They have been carried out using a SETARAM TG/DSC instrument (with alumina crucible as reference) Model 92-1750 to observe the decomposition behaviour and the lowest calcination temperature for each composition. These analyses have been undertaken in a flowing air atmosphere, from room temperature (RT) to 1400 °C, with a heating and cooling rate of 10 °C min^{-1}. Specific surface area of each powder, obtained by calcination of the freeze-dried precursors at two different temperatures (900 °C and 1000 °C for 4 h) were measured by N_2 adsorption (BET method) with a monosorb SA (Surface Area) 3100 instrument and using a N_2/He gas mixture. Powders (∼300 mg) were first dried and degassed under vacuum, at 100 °C for an outgas time of ∼17 h. Average particle sizes (d_{BET}) were calculated from an equation corresponding to Brunauer, Emmett et Teller (BET) theory [40]. Phases were identified by X-ray powder diffraction. Each pattern was recorded in air and at RT, in a Bragg–Brentano θ–2θ configuration. The wavelength used was Cu $K_{\alpha 1 + 2}$ filtered with a nickel foil to remove Cu K_{β} wavelength. Data were collected in the 2θ region between 10° and 110° with a 0.02° 2θ-step and 10 s/step of acquisition. Le Bail refinements, carried out using the program FULLPROF [41] and its interface WinPLOTR [42], were based on the cell parameters determined by M. A. G. Aranda and al. [43] for the $La_{9.33}Si_6O_{26}$ compound and using neutron diffraction. A pseudo-Voigt function was used as the profile function. Samples' morphology was observed using a FEG (LEO 1530) scanning electron microscope operating at 5 kV. At the same time, energy dispersive X-ray (EDX) spectra were systematically recorded with a link system digital spectrometer PGT (Princeton Gamma Tech, PRISM) on randomly chosen particles to control compositional homogeneity before and after sintering. For microstructural characterisations of sintered bodies, surfaces were previously polished using SiC papers until surfaces of optical quality were obtained. Grain boundaries were then revealed by thermal etching, 50 °C below the sintering temperature for 5 min with a heating scan of 2 °C min^{-1}. To allow their observation, a fine layer of gold metal was deposited onto these samples by radio frequency sputtering.

2.4. Electrical measurements

Electrical properties were investigated by impedance spectroscopy using a model 1260 high-frequency response analyzer of M/s Solartron (Schlumberger, UK) with a 50 mV amplitude ac voltage over the 0.10 Hz–10 MHz frequency range. Measurements were performed in air, on dense samples (>95% of relative densities) between 200 °C and 700 °C with a 25 °C-step. Several impedance measures were taken to guarantee reproducibility. Electrodes were painted on the polished faces of the samples with a Pt paste (METALOR n° 6926) and then heat-treated at 1000 °C during 1 h. Samples were then measured inside a commercial sample holder (Ionic-systems) in a four-wire (Pt)

configuration. The contact between electrodes and wires being ensure by platinum foil current collectors. Data collection was performed after being sure that the impedance at fixed frequency and temperature have been stabilized. Impedance complex data were analyzed either by extracting, at each temperature, total resistances from the intercept of the high frequency semi-circle with the x-axis or by fitting data with equivalent circuit using Zview™ software.

3. Results and discussion

3.1. Characteristics and decomposition of freeze-dried precursor

Whitish fine and highly dispersed precursors were obtained after freeze-drying. At first sight, they contained a high amount of organic residues and the XRD patterns (not represented here because of the absence of diffraction peaks) reflected the amorphous nature of these powders. These dried precursors were then subjected to TG/DSC analysis. The TG curves displayed in Fig. 2 show that the decomposition, associated with an important weight loss ($\sim 45\%$) regardless of composition, occurs in several steps between RT and 900 °C. The DSC (see inset in Fig. 2) reveals the presence of two strong exothermic peaks at 330 °C, 380 °C and a weak one at 800 °C indicating several steps in the decomposition's mechanism of organic species over this temperature range. The last weight loss was observed at approximately 870 °C. From temperatures above 900 °C, it could be assumed that all organic species were decomposed, presumably leading to pure oxy-apatite materials, the composition of which would then remain unchanged up to 1400 °C. However, there is evidence for oxy-apatite formation in TG and DSC experimental results: DSC signal allotted to apatite phases crystallization was observed at 800 °C. XRD pattern, recorded at this temperature but not represented here, testified to crystallisation of oxy-apatite materials. From 800 °C, a mixture of apatite and amorphous phases are obtained. Given these observations, all dried precursors were calcined at 900 °C or 1000 °C for 4 h in order to obtain well-crystallized oxy-materials. This calcination temperature was reached with a
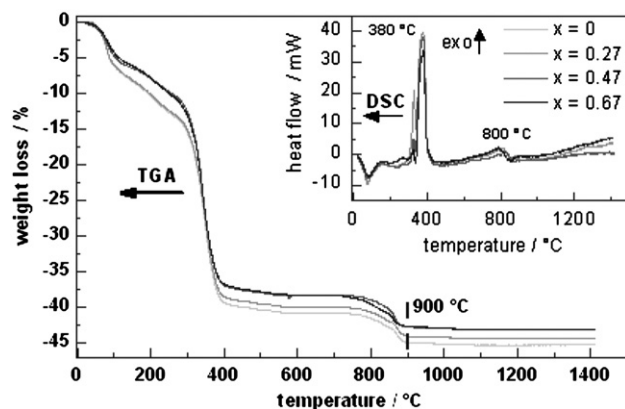
Fig. 2. TG curves of dried-precursors prepared by freeze-drying and further heated for 4 h at 900 °C (DSC curves associated to decomposition was represented in inset).
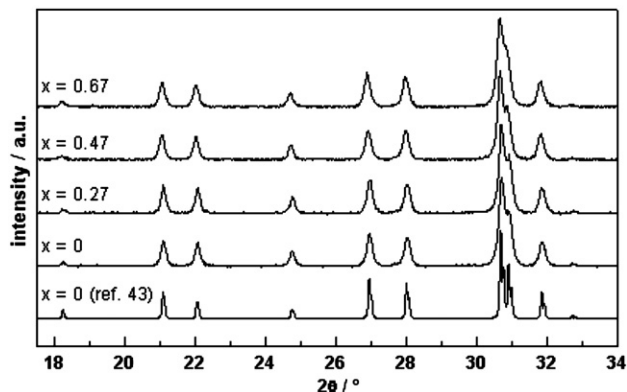
Fig. 3. XRD patterns of oxy-apatite materials compared with a simulation [43]. based on crystallographic data (for $La_{9.33}Si_6O_{26}$) extracted from neutron diffraction pattern by M. A. G. Aranda et al.

heating rate of 5 °C min^{-1} and the temperature drop was obtained by switching off the furnace.

3.2. Characteristics of oxy-apatite nanopowders

X-ray diffraction patterns of samples heat-treated at 900 °C are displayed in Fig. 3. These diagrams compare very well to the simulated one [43] ($x=0$; ref. 43) revealing that at 900 °C, the expected oxy-apatite materials were produced with no impurities such as La_2SiO_5 or $La_2Si_2O_7$. In Fig. 3, diffraction peaks' width accounts for the very small size of the crystallites obtained after calcination. Le Bail fitting of these diffraction patterns have been carried out in the space group $P6_3/m$ starting from the cell parameters of $La_{9.33}Si_6O_{26}$ [43]. Results, gathered in Table 1, show a slight increasing of cell volume with lanthanum content and are similar to those encountered in literature [17,23,43,44,49,50]. Similar results were obtained for the samples calcined at 1000 °C. Thus, it can be mentioned that freeze-dried precursors, as those obtained by sol–gel methods [21,25], turn out into well-crystallized oxy-apatite materials by calcination at temperatures rather lower than what is currently reported for solid state reaction [15,16,44]. Besides, the fact that single phases of $La_{9.33+x}(SiO_4)_6O_{2+3x/2}$ oxy-apatites were observed at 900 °C and 1000 °C would indicate that for low temperatures (or small grains' size) oxy-apatite phases are thermodynamically stable in the whole compositional range of $9.33 \leq 9.33+x \leq 10.0$. Another explanation could be that a secondary amorphous phase is present and crystallizes only at higher temperature. Considering microstructural aspects, the powders calcined at 900 °C and at 1000 °C present a relatively high specific surface (Table 2). These values, ranging from 8.0

Table 1
Cell parameters of $La_{9.33+x}(SiO_4)_6O_{2+3x/2}$ compounds (obtained at 900 °C) as a function of x

x	$a/\text{Å}$	$b/\text{Å}$	$V/\text{Å}^3$
0	9.7267(7)	7.1916(6)	589.23(8)
0.27	9.7311(7)	7.1950(6)	590.05(8)
0.47	9.7326(7)	7.1952(6)	590.24(8)
0.67	9.7393(9)	7.2071(6)	592.04(8)

Table 2
Effects of 900 °C or 1000 °C calcination temperature on specific surface area of the as-synthesized powders

x	$S_{BET}/m^2\,g^{-1}$ (900 °C)[a]	d_{BET}/nm (900 °C)[b]	$S_{BET}/m^2\,g^{-1}$ (1000 °C)[a]	d_{BET}/nm (1000 °C)[b]
0	14.2(1)	80(1)	11.3(1)	100(1)
0.27	13.2(1)	84(1)	11.0(1)	100(1)
0.47	12.4(1)	88(1)	8.2(1)	130(1)
0.67	14.8(1)	73(1)	10.9(1)	98(1)

[a]Measured by BET method; [b]calculated from the BET's law.

(1) m^2 g^{-1} to 15.0(1) m^2 g^{-1} regardless of composition, are inversely correlated to the calcination temperature. Scanning electron micrographs, displayed in Fig. 4, illustrate the morphology of a La$_{9.60}$Si$_6$O$_{26.4}$ powder prepared by calcination of the precursor at 900 °C for 4 h. In this figure, the divided aspect of the powder can be appreciated. It consists in soft agglomerates of small entangled-rods the size of which range between 100 and 200 nm in length. The nanometric nature of these powders is also reflected by the equivalent particles' size as calculated from BET's equation and given in Table 2. In our case and contrary to traditional sol–gel processes, particles are not strongly agglomerated. This characteristic can be attributed to the fast kinetics of the precursor's decomposition below 400 °C. Indeed, the high intensity of the DSC peak, observed at this temperature, establishes its vigorous nature. Then, gases' evolution during decomposition steps prevents particles from a possible agglomeration: this phenomenon is usually encountered during auto-ignition synthesis [45]. This may partly account for the densification improvement observed and detailed below.

3.3. Characteristics of sintered oxy-apatite samples

It can therefore be wondered whether these nanopowders become compact materials after sintering since these compositions are well-known to present a strong aversion against densification. Two strategies were thus designed in order to sinter these materials, one using conventional sintering at high temperature and the other one by SPS.
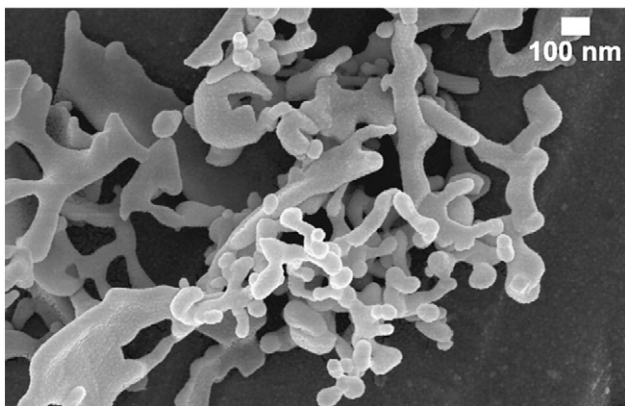

Fig. 4. SEM micrograph of La$_{9.60}$Si$_6$O$_{26.4}$ powder after calcination of the freeze-dried precursor at 900 °C for 4 h.
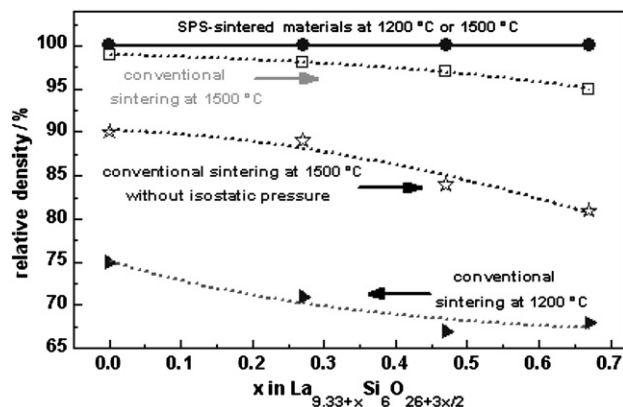

Fig. 5. Evolution, as a function of composition, of relative densities for SPS-sintered materials at 1200 °C and 1500 °C (●) compared to those obtained by conventional sintering at the same temperature for 12 h (✳: without isostatic pressing).

3.3.1. Conventional sintering

A first step has consisted in determining the optimal conventional sintering temperature which leads to compact materials with a density at least equal to 95% (required for the desired application). After testing several temperatures, we observed that increasing the lanthanum content tends to decrease the final density. For instance, the difference in compactness between La$_{9.33}$Si$_6$O$_{26}$ and La$_{10}$Si$_6$O$_{27}$ compounds after a sintering at 1400 °C amounts to 11 points (98% versus 87% respectively). Then, a 1500 °C sintering temperature allows at obtaining a full series of samples with density higher than 95%. Indeed, after a 1500 °C sintering, samples had relative densities of 99%, 98%, 97% and 95% for La$_{9.33}$Si$_6$O$_{26}$, La$_{9.60}$Si$_6$O$_{26.4}$, La$_{9.80}$Si$_6$O$_{26.7}$ and La$_{10}$Si$_6$O$_{27}$, respectively (see Fig. 5). By comparison, A. Vincent and al. [20] have reported a density of 98% for La$_{9.33}$Si$_6$O$_{26}$ but at a 1600 °C sintering temperature. It is also interesting to note that the optimal density of 95% could be obtained for La$_{9.33}$Si$_6$O$_{26}$ material at a sintering temperature of only 1350 °C. This temperature is lowered from at least 200 °C compared to that which is currently reported in the literature to obtain a similar density values. It can finally be noticed that all dense pellets obtained after sintering at 1500 °C for 12 h present a noticeable vitreous aspect. In Fig. 6 are represented electron micrographs of La$_{9.33+x}$Si$_6$O$_{26+3x/2}$ ($0 \leq x \leq 0.67$) materials sintered at 1500 °C for 12 h which have been represented at the same scale for comparison. These images clearly reflect their dense microstructure consisting in grains whose the size ranges from 0.5 to 5 μm and delimited by well-defined grain boundaries. Micrographs also show a slight increase of remaining porosity with lanthanum content in good agreement with density evolution curves displayed in the Fig. 5. This density's evolution with composition might be related first to the presence of more cation-vacancies in La-poor samples which may favour cation diffusion and then to the presence of La$_2$SiO$_5$ in La-rich samples which can hinder sintering. Further studies would be necessary to confirm this last assumption. Finally, another experiment was realized to determine whether isostatic pressing significantly improves densification. Pellets were therefore treated by uniaxial pressing only and sintered at 1500 °C for 12 h. Results shown in Fig. 5 illustrate that isostatic pressing before sintering is decisive,
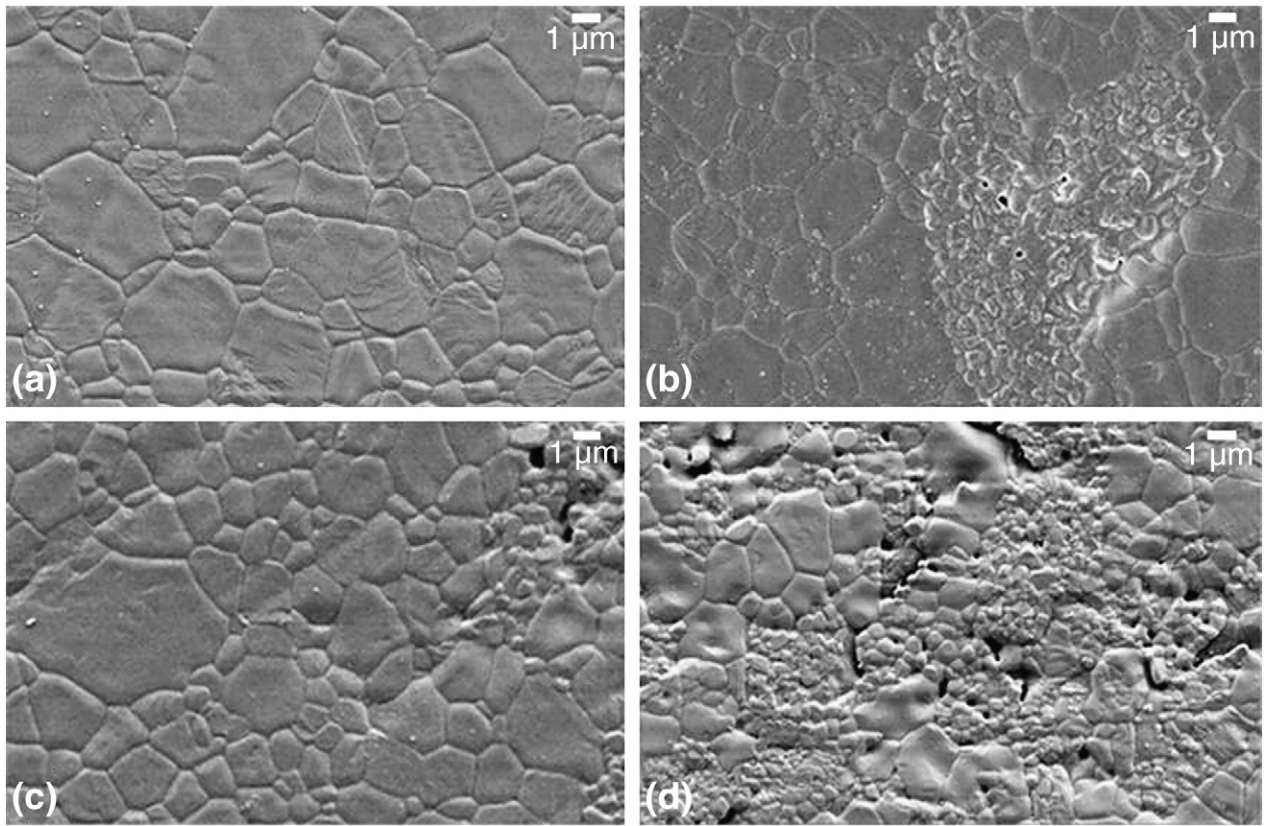
Fig. 6. SEM micrographs of samples prepared by conventional sintering at 1500 °C during 12 h. (a) $La_{9.33}Si_6O_{26}$, (b) $La_{9.60}Si_6O_{26.4}$, (c) $La_{9.80}Si_6O_{26.7}$ and (d) $La_{10}Si_6O_{27}$.

especially as lanthanum content increases. Nevertheless, the present study has demonstrated that the successfull combination of freeze-drying and conventional sintering can lead to dense material at a rather low temperature. X-ray diffraction on these dense pellets sintered at 1500 °C for 12 h (Fig. 7) reveals that from $x=0.47$, La_2SiO_5 appears as an impurity phase along with the apatite phase as the major compound. This means that for $x \geq x_{lim}$, x_{lim} being superior or equal to 0.27, a mixture of the two phases is obtained.

Similarly, Aranda and al. [15] have reported the existence of oxy-apatite as single phases in the range $0 \leq x \leq 0.29$. However, we showed that single phase powders could also be obtained for $x > 0.27$ after a calcination at 900 °C of freeze-dried precursors. These experiments thus seem to show that the existence domain of the solid solution $La_{9.33+x}Si_6O_{26+3x/2}$ is reduced on the La-rich side

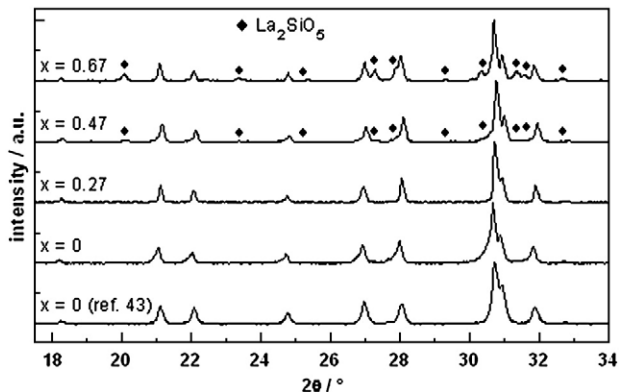Fig. 7. XRD patterns of $La_{9.33+x}(SiO_4)_6O_{2+3x/2}$ dense materials (sintered at 1500 °C for 12 h) compared with that of $La_{9.33}Si_6O_{26}$ obtained after calcination at 900 °C for 4 h (♦ La_2SiO_5 phase formation).
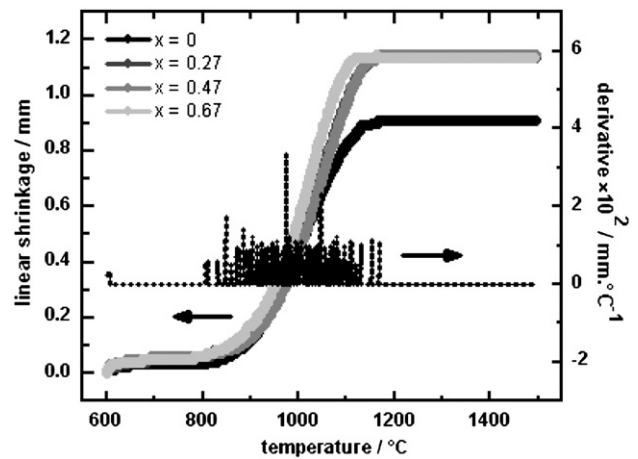

Fig. 8. Linear shrinkage curves in a function of temperature for $La_{9.33+x}$ $(SiO_4)_6O_{2+3x/2}$ ($0 \leq x \leq 0.67$) compounds subjected to SPS at 100 MPa pressure and one derivative for $La_{9.33}Si_6O_{26}$ as a representative example of maximum shrinkage rate.

of the binary La_2O_3–SiO_2 phase diagram when temperature increases from 900 °C to 1500 °C.

3.3.2. Spark plasma sintering at 1200 °C and 1500 °C

In Fig. 8 is presented the linear shrinkage of sample during SPS sintering while a pressure of 100 MPa was continuously applied. Regardless of composition, shrinkage curves follow almost the same behaviour with temperature. According to derivative curves, displayed for $La_{9.33}Si_6O_{26}$ material (dotted line in Fig. 8), shrinkage takes place at around 800 °C, is significant at 975 °C and is achieved at 1180 °C, this temperature from which a complete densification is awaited. Therefore, considering sintering temperatures which have been implemented in this case, *i.e.* 1200 °C and 1500 °C, highly dense ceramics should be obtained and relative densities of 100% are expected. Indeed, in Fig. 9a and b, photographs allow us to appreciate optical transparency of $La_{9.60}Si_6O_{26.4}$ and $La_{9.80}Si_6O_{26.7}$ SPS-sintered samples (representative of the sample aspect in the course of this study) at 1500 °C which reflects their whole densification. Indeed, optical opacity is mainly due to microstructural effects, such as micro-porosity, composition's inhomogeneity, micro-defects and micro-strains. These microstructural's imperfections, which precipitate at grain boundaries, are responsible for light scattering. For instance, it has been reported that obtention of transparent materials [46] remains difficult if not impossible when fraction of porosity is over 1% in dense ceramic's volume. For instance, Fig. 10a and b illustrates surface's microstructure of both transparent SPS-sintered materials
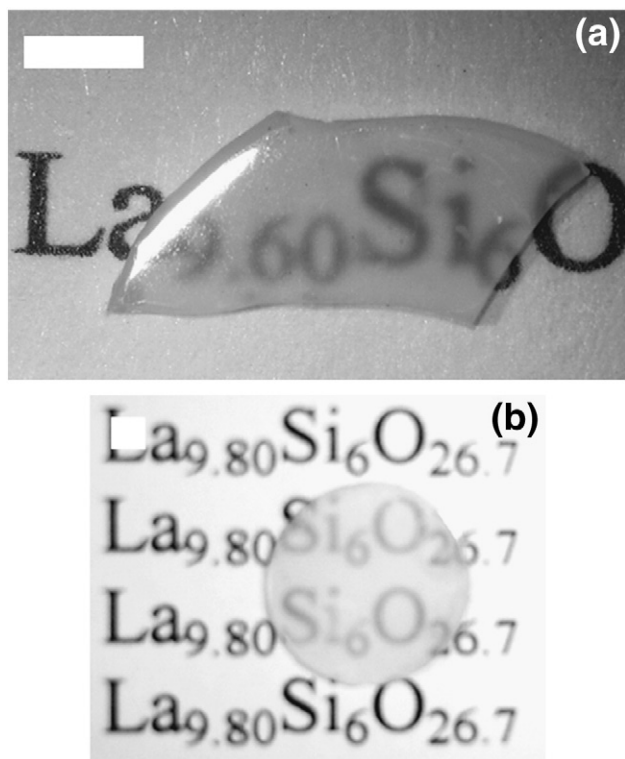

Fig. 10. SEM photographs showing of fully dense ceramics of (a) $La_{9.60}Si_6O_{26.4}$ and (b) $La_{9.80}Si_6O_{26.7}$ SPS-sintered at 1500 °C (micrographies have been recorded on the surface of oxy-apatite materials display in Fig. 9).

Fig. 9. Photographs showing the transparency of SPS-sintered bodies for (a) $La_{9.60}Si_6O_{26.4}$ at 1500 °C and (b) $La_{9.80}Si_6O_{26.7}$ at 1500 °C. Samples are around 0.5 mm thick and were polished using SiC sandpapers (white straight line corresponds to a 1 mm drawing scale).
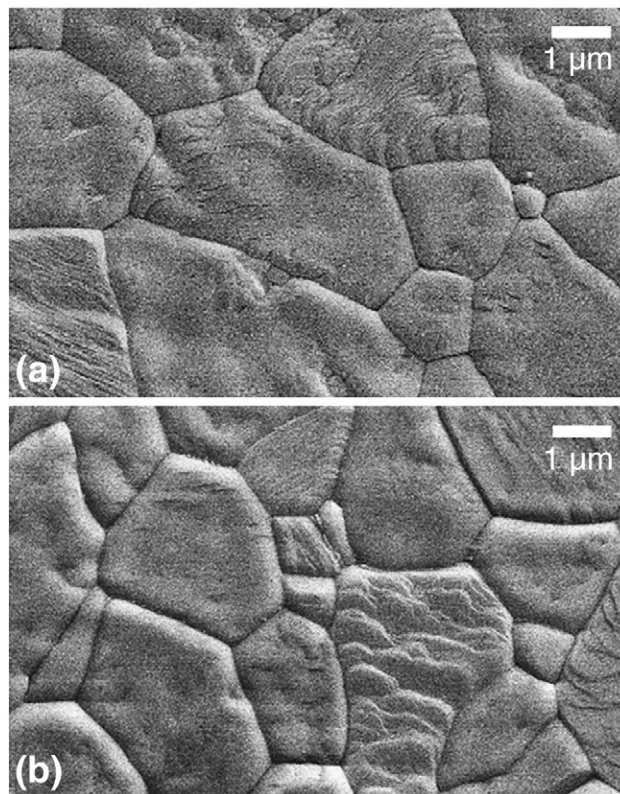
at 1500 °C, represented in Fig. 9a and b respectively. In fact, relative densities as measured from weight to volume ratio are 100% regardless of composition. Then, the differences of efficiency between conventional and Spark Plasma sintering are clearly demonstrated in Fig. 5 by comparing densities obtained form both methods at the same temperatures (1200 °C and 1500 °C). For instance, densities ranging from 65% to 75% were obtained by conventional sintering at 1200 °C for 12 h while 100% were reached by SPS at 1200 °C for 3 min. However, at 1500 °C, the advantage of SPS over conventional sintering becomes negligible in terms of densities (100% versus >95%). The high level of compactness reached with SPS could be attributed to the beneficial effect of contineous applied pressure or to an additional effect of electric field during SPS. Another interesting characteristic of SPS samples is the strong difference of microstructure between those samples sintered at 1200 °C with those sintered at 1500 °C as shown in a previous article [47]. While the relative density is 100% in both cases, the sample sintered at 1200 °C presents an average grains' size of 100–500 nm range versus 1-5 µm for the one sintered at 1500 °C, that is to say 10 time bigger. Unsurprisingly, linear shrinkage curves for $La_{9.33+x}Si_6O_{26+3x/2}$ ($0 \leq x \leq 0.67$), in Fig. 8, have illustrated that 1200 °C corresponds to the temperature from which densification was theoretically achieved. Thus, when samples' shrinkage becomes nil, an increase in temperature will result essentially in grain's growth. These results clearly demonstrate that SPS enables to control ceramics' microstructure while maintaining a high densification level in these

materials prone to porosity. X-ray diffraction studies have been undertaken on SPS-sintered materials at 1200 °C. Similarly to conventionally sintered samples, pure oxy-apatite materials were only obtained for $x \le 0.27$. For higher values of x, extra peaks corresponding to the parasitic phase La_2SiO_5 were observed (Fig. 11). Such results indicate that it remains possible, at high temperature, to stabilize compounds of the solid solution $La_{9.33+x}Si_6O_{26+3x/2}$ at least up to $x=0.27$. Le Bail refinements have been carried out in order to follow cell parameters (Table 3) versus composition. The observed, calculated and X-ray diffraction profiles for $La_{9.33+x}Si_6O_{26+3x/2}$ ($0 \le x \le 0.67$) materials are shown in Fig. 11. For $x=0.47$ and $x=0.67$, all diffraction patterns are explained taking La_2SiO_5 (SG $P2_1/c$; a=9.3153(5) Å, b=7.4991(5) Å, c=7.0359(6) and β=108.64 (1) °) into consideration for refinements. Cell parameters for $La_{9.33+x}Si_6O_{26+3x/2}$ materials do not evolve much with composition so that values are similar to those reported in literature [17,23,43,48–50].

3.4. Electrical measurements

All the samples used for electrical measurements have relative densities above 95%. Since they are wholly dense, accurate

Table 3
Cell parameters of $La_{9.33+x}Si_6O_{26+3x/2}$ ($0 \le x \le 0.67$) compounds (sintered at 1500 °C for 0 min) as a function of x

x	a/Å	b/Å	V/Å^3
0	9.7224(2)	7.1830(2)	588.00(3)
0.27	9.7192(3)	7.1857(2)	587.85(3)
0.47	9.7227(2)	7.1841(2)	588.13(3)
0.67	9.7261(2)	7.1827(3)	588.43(3)

measurements can be performed and will be representative of oxy-apatite materials. In this case, either grains' size or ceramics' composition alone will be variable parameters which are likely to affect anionic mobility. Impedance data (corrected by the shape factor e/S (in cm^{-1}) of the sample) are displayed in the form of Nyquist plots (Fig. 12) for $La_{9.33}Si_6O_{26}$ SPS-sintered (1200 °C (open circles) and 1500 °C (open squares)) at different temperatures from 300 °C and 620 °C. These impedance data are representative of all samples investigated in the course of this study. At low temperature, electrical response of samples essentially consists in one depressed arc at high frequency (in the 10^2-10^7 Hz frequency range) plus the electrode contribution as a spike inclined at roughly 45 °, at low frequency (<10^2 Hz) (Fig. 12 a–c). Such depression usually implies that relaxation
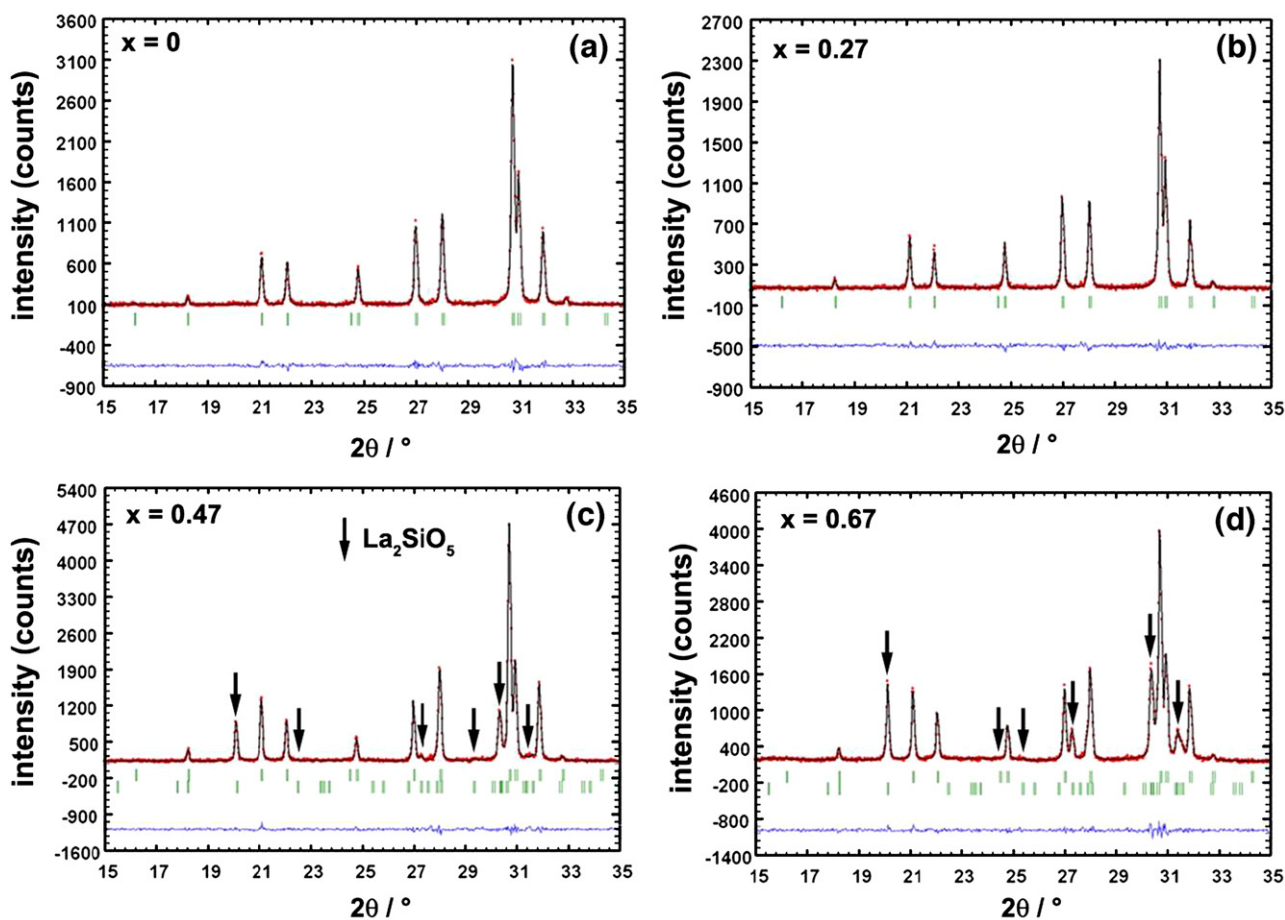

Fig. 11. Observed (red closed circles), calculated (solid line), Bragg reflexions (green vertical ticks) and difference (blue line) powder diffraction profiles for (a) $La_{9.33}Si_6O_{26}$, (b) $La_{9.60}Si_6O_{26.4}$, (c) $La_{9.80}Si_6O_{26.7}$ and (d) $La_{10}Si_6O_{27}$ SPS-sintered bodies at 1200 °C for 3 min. La_2SiO_5 (↓) appears as an impurity phase resulting from the decomposition of oxyapatite for $x>0.27$. (For interpretation of the references to color in this figure legend, the reader is referred to the web version of this article).
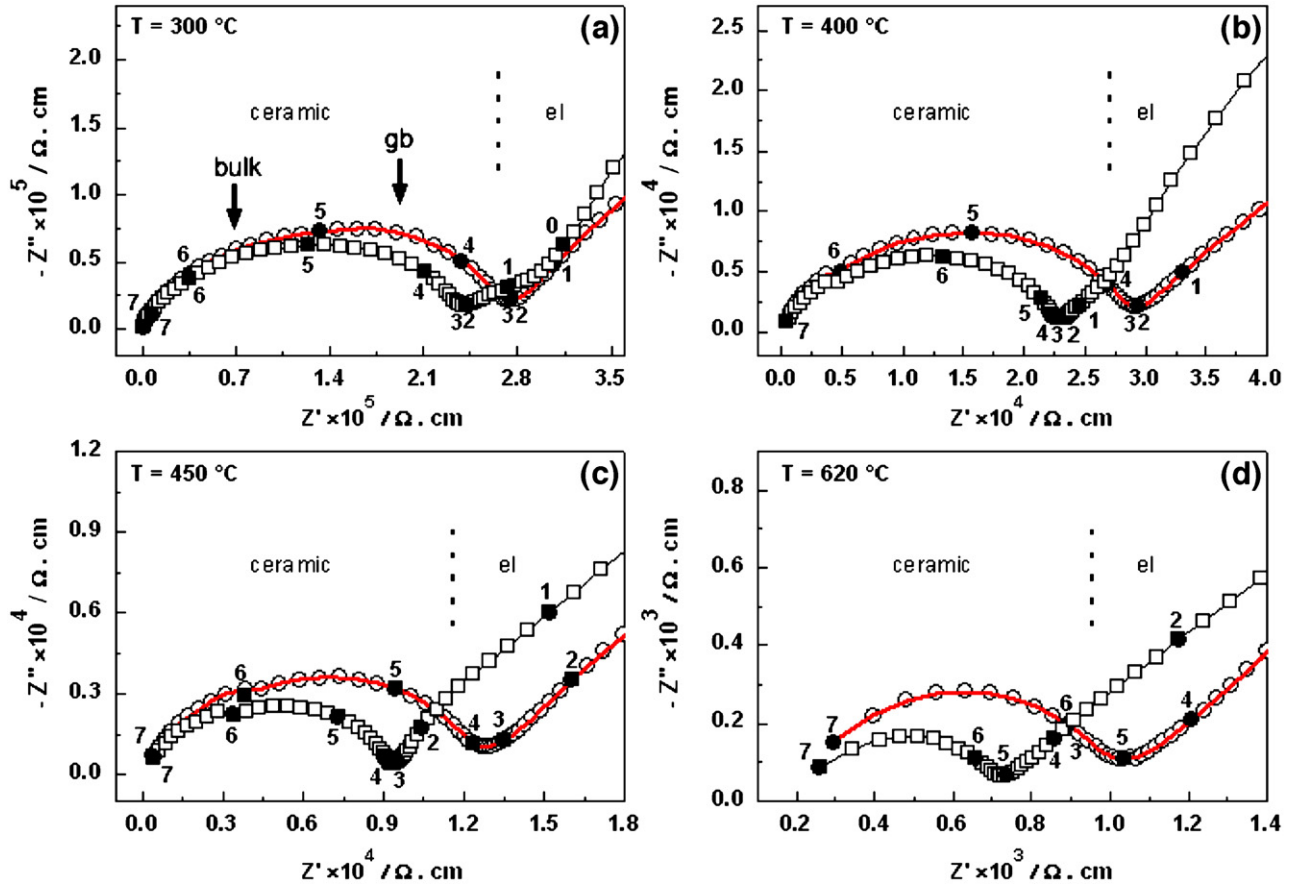
Fig. 12. Complex impedance spectra at different temperatures (figures on curves denote decades of frequency) for La$_{9.33}$Si$_6$O$_{26}$ SPS-sintered at 1200 °C (○) and 1500 °C (□): (a) T=300 °C, (b) T=400 °C, (c) T=450 °C and (d) T=620 °C (the red solid lines are the fittings). (For interpretation of the references to color in this figure legend, the reader is referred to the web version of this article).

times are not alone defined for these samples, but rather are distributed in a broad frequency band. Ceramics electrical response might be constituted of two processes ('b': bulk and 'gb': grain boundaries) that are difficult to separate when strongly overlapped. Some attempts has been made to distinguish both contributions. In this case, impedance spectra were modelled using an equivalent electrical circuit formed with the series association of two parallel R$_i$C$_i$ circuits. The least-squares fitting (electrical response of SPS-sintered sample at 1200 °C as an example) leads to capacitances C$_b$ ≈ 35 pF.cm^{-1} (the shape factor of the sample is 0.39 cm^{-1}) and C$_{gb}$ ≈ 0.20 nF.cm^{-1}, which are in good agreement, respectively, with bulk (high frequency semicircle) and grain boundaries' (intermediate frequency semicircle) capacitances already encountered in such materials [16,25,51]. These values show that bulk and grain boundaries' relaxation frequencies are very close each other with a ratio of ~5.7. At high temperature (>450 °C), only one contribution associated to the material response can be observed (Fig. 12d) and the vertical spike at lower frequency (<10^5 Hz) turns into a broad semicircle which translates the diffusion-limited processes at the electrodes. The later can be modelled by a short Warburg (W$_s$) electrical component. For our study, the difficulty to resolve both grain and grain boundaries' processes at high temperature led us to consider only total resistance in impedance spectra even at intermediate temperatures. Actually, the total resistance value is the

only significant value when considering the application. Impedance spectra presented in Fig. 12 do not show an important resistivity variation between both samples. This is all the more surprising that grains in La$_{9.33}$Si$_6$O$_{26}$ SPS-sintered materials at 1200 °C and 1500 °C differ by more than a factor 10 in size. This

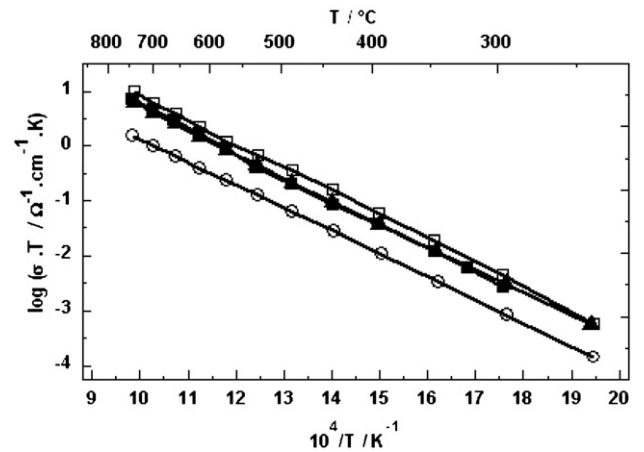Fig. 13. Temperature dependence of the overall electrical conductivity for La$_{9.33+x}$(SiO$_4$)$_6$O$_{2+3x/2}$ (0 ≤ x ≤ 0.67) SPS-sintered materials at 1500 °C for 0 min in a function of x: La$_{9.33}$Si$_6$O$_{26}$ (▲), La$_{9.60}$Si$_6$O$_{26.4}$ (□), La$_{9.80}$Si$_6$O$_{26.7}$ (■), La$_{10}$Si$_6$O$_{27}$ (○).

Table 4
Total activation energy associated to anionic conductivity of $La_{9.33+x}Si_6O_{26+3x/2}$ $(0 \leq x \leq 0.67)$ materials conventionally and SPS-sintered, as a function of x

$9.33+x$	E_a (eV) (in the 400 °C-700 °C temperatures' range)		
	SPS (1200 °C)	SPS (1500 °C)	Conv. (1500 °C)
9.33	0.87(5)	0.89(5)	0.79(5)
9.60	0.90(5)	0.87(5)	0.83(5)
9.80	0.91(5)	0.85(5)	0.83(5)
10.0	0.89(5)	0.83(5)	0.83(5)

would signify that nanometric oxy-apatite samples could have levels of conduction almost similar to those of micronic samples, reflecting the possible insignificant contribution of grains' boundaries. Fig. 13 resumes the electrical response of SPS-sintered materials at 1500 °C in the form of Arrhenius' plots *i.e.* log $(\sigma_{tot}.T)$ versus 1/T. We dot not observe strong differences between the different samples and a same behaviour was observed for the other series of samples prepared by SPS at 1200 °C or by conventional sintering at 1500 °C. From the slope of these straight lines, it is possible to extract total activation energies associated with oxide ion mobility (Table 4) for SPS-and conventionally-sintered materials. For all SPS-sintered materials either at 1200 °C or at 1500 °C, they range from 0.83(5) eV to 0.91(5) eV depending on La-content and are closely similar to those previously reported [11,14]. However, at fixed composition, activation energy is slightly smaller for the conventionally-sintered material which contains bigger grains' size. The minimum total activation energy of 0.79(5) eV obtained for $La_{9.33}Si_6O_{26}$ conventionally-sintered is similar to that one previously reported *i.e.* 0.74(5) eV [48] but conversely lower than 0.87(5) eV [25] and 0.90(5) eV [20] also mentioned for the same material. For $x \geq 0.27$, E_a values are slightly higher than the one determined for $La_{9.33}Si_6O_{26}$ and remain identical to ~0.83(5) eV. One can point out it that $La_{9.33}Si_6O_{26}$ presents the higher density of 99% with respect to the other materials for a 1500 °C sintering temperature and minor increasing in porosity should slightly affected activation energy. Evolution of total conductivity according to the composition is displayed in Fig. 14 at $T=700$ °C for SPS- and conventionally-sintered bodies. This curve shows that, for SPS-sintered materials, total conductivity increases with x, reaches the maximum value at $x=0.27$, then continuously decreases up to $x=0.67$. Some features could explain this evolution of σ_{tot} with the composition. Since materials are fully dense (100%), conductivities' evolution are solely composition dependent for definite microstructure. Below $x=0.27$, while single phases of oxy-apatite materials were obtained after sintering (Fig. 11), conductivity improvement could be attributed to additional oxygen arising from lanthanum insertion in the oxy-apatite structure. For $x>0.27$, the non-conducting La_2SiO_5 secondary phase which appears during sintering step at high temperature allows to explain conductivity drop. For conventionally-sintered materials, continuous decreasing of the overall conductivity with composition can be explained as a consequence of a predominant effect of porosity (Fig. 6). However, they display almost similar conductivity values than those of SPS-sintered ones. This result is not surprising considering that grains' size of SPS-sintered materials are roughly smaller than those of conventionally sintered. The overall conductivity at 500 °C for $La_{9.33}Si_6O_{26}$

conventionally-sintered, $\sigma_{500\ °C}=6.44.10^{-4}$ S cm^{-1}, is higher than the ones reported in the literature *i.e.* $7.2.10^{-5}$ S cm^{-1}[24], $7.31.10^{-5}$ S cm^{-1} [25], $1.13.10^{-4}$ S cm^{-1} [19] for the same material. At 700 °C, its reaches $\sigma_{700\ °C}=7.33.10^{-3}$ S cm^{-1} by comparison with $1.2.10^{-4}$ S cm^{-1} [48], 2.10^{-4} S cm^{-1} [16] and 3.10^{-4} S cm^{-1} [20] previously reported. High densities obtained for the present material implies conductivities' values higher than those mentioned in the literature. Conductivity data reveal that the highest value at 700 °C, $\sigma_{700\ °C}=7.33.10^{-3}$ S cm^{-1} was reached for $La_{9.33}Si_6O_{26}$ sample whose density is equal to 99%. In this study, $La_{10}Si_6O_{27}$ is the sample which present the lower conductivity with $\sigma_{500\ °C}=1.45.10^{-4}$ S cm^{-1} at 500 °C and $\sigma_{700\ °C}=1.39.10^{-3}$ S cm^{-1} at 700 °C while S. Nakayama and al. [7] have reported $4.3.10^{-3}$ S cm^{-1} and $1.1.10^{-2}$ S cm^{-1}, respectively. For this material the value $\sigma_{500\ °C}=1.45.10^{-4}$ S cm^{-1} is in good accord with $1.63.10^{-4}$ S cm^{-1} mentioned by J. T. S. Irvine and al. [25] and slightly higher because of the more important compactness of the sample. Nevertheless, for $x>0.27$, important precautions must be taken in the interpretation of conductivities' data insofar as both effects, porosity and secondary phase interfere like variables. Both the formation of the latter and the decreasing in anionic conductivity implies that pure apatite-type $La_{10}Si_6O_{27}$ could not be prepared in the course of this study.

4. Conclusion

An efficient and original wet-chemical synthesis by freeze-drying was used for elaboration of oxy-apatite. Electron micrographies have shown that powders consist in soft agglomerates of particles whose size range from 100 to 200 nm after a 900 °C calcination of freeze-dried precursors. The nanometric features of these powders as their specific surface area (>12.4 m^2 g^{-1}) predict a very high reactivity to conventional sintering at high temperature. Indeed, the results that we are showing in the paper are very convincing since high density (>95%) materials were obtained at rather lower temperature (≤ 1500 °C) than what is currently reported in literature (~1700 °C) to reach comparable levels of
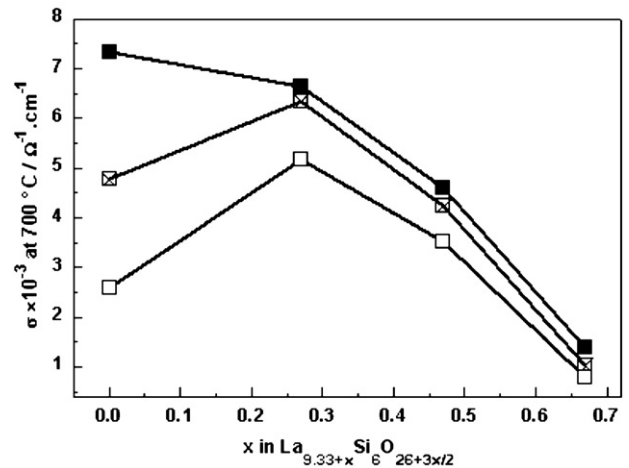

Fig. 14. Evolution of the overall conductivity vs. x at 700 °C for dense $La_{9.33+x}(SiO_4)_6O_{2+3x/2}$ $(0 \leq x \leq 0.67)$ materials: SPS-sintered at 1200 °C for 3 min (□), SPS-sintered at 1500 °C for 0 min (⊠), conventionally sintered at 1500 °C for 15 h (■).

compactness. Results have demonstrated that densification rate was narrowly correlated to sintering temperature and lanthanum content. A powerful technique by Spark Plasma sintering (SPS) has led to wholly dense (100% of the theoretical density) and translucent materials. The present work has demonstrated the successful combination of freeze-drying and SPS processes for the densification of hard-to-sinter oxy-compounds. It has been shown that SPS allows to significantly reduce sintering temperatures (*i.e.* 1200 °C instead of 1500 °C) while operating for shorter time (3 min vs. 12 h), compared to those conventionally used. Electrical measurements have shown that conductivity behaviour is mainly composition-dependent and its decrease for $x > 0.27$ could be attributed to La_2SiO_5 ion's blocking phase. The highest overall conductivity reached at 700 °C, *i.e.* $\sigma_{700 \,°C} = 7.33.10^{-3}$ S cm^{-1}, is obtained for $x = 0$ conventionally-sintered material.

Acknowledgements

References

[1] S.P.S. Badwal, F.T. Ciacchi, Adv. Mater. 13 (2001) 1993.
[2] B.C.H. Steele, J. Mater. Sci. 36 (2001) 1053.
[3] O. Yamamoto, Electrochim. Acta 45 (2000) 2423.
[4] N.Q. Minh, J. Am. Ceram. Soc. 76 (1993) 563.
[5] A.J. McEvoy, Solid State Ionics 132 (2000) 159.
[6] J. Drennan, G. Auchterlonie, Solid State Ionics 134 (2000) 75.
[7] S. Nakayama, M. Sakamoto, J. Eur. Ceram. Soc. 18 (1998) 1413.
[8] S. Nakayama, T. Kageyama, H. Aono, Y. Sadaoka, J. Mater. Chem. 5 (1995) 1801.
[9] S. Nakayama, H. Aono, Y. Sadaoka, Chem. Lett. 24 (1995) 431.
[10] A.S. Risbud, K.B. Helean, M.C. Wilding, P. Lu, A. Navrotsky, J. Mater. Res. 16 (2001) 2780.
[11] S. Nakayama, M. Sakamoto, J. Mater. Sci. Lett. 20 (2001) 1627.
[12] E.J. Abram, D.C. Sinclair, A.R. West, J. Mater. Chem. 11 (2001) 1978.
[13] A.N. Christensen, R.G. Hazell, A.W. Hewat, Acta Chem. Scand. 51 (1997) 37.
[14] A.L. Shaula, V.V. Kharton, F.M.B. Marques, J. Solid State Chem. 178 (2005) 2050.
[15] L. León-Reina, E.R. Losilla, M. Martínez-Lara, S. Bruque, M.A.G. Aranda, J. Mater. Chem. 14 (2004) 1142.
[16] P.J. Panteix, I. Julien, D. Bernache-Assollant, P. Abélard, Mater. Chem. and Phys. 95 (2006) 313.
[17] J.E.H. Sansom, E. Kendrick, J.R. Tolchard, M.S. Islam, P.R. Slater, J. Solid State Electrochem. 10 (2006) 562.
[18] A. Najib, J.E.H. Sansom, J.R. Tolchard, P.R. Slater, M.S. Islam, Dalton Trans. (2004) 3106.
[19] J.E.H. Sansom, J.R. Tolchard, P.R. Slater, M.S. Islam, Solid State Ionics 167 (2004) 17.
[20] A. Vincent, S. Beaudet Savignat, F. Gervais, J. Eur. Ceram. Soc. 27 (2007) 1187.
[21] S. Célérier, C. Laberty-Robert, F. Ansart, C. Calmet, P. Stevens, J. Eur. Ceram. Soc. 25 (2005) 2665.
[22] S. Célérier, C. Laberty, F. Ansart, P. Lenormand, P. Stevens, Ceram. Inter. 32 (2006) 271.
[23] H. Yoshioka, J. Alloys Comp. 408-412 (2006) 649.
[24] Y. Masubuchi, M. Higuchi, T. Takeda, S. Kikkawa, J. Alloys and Comp. 408-412 (2006) 641.
[25] S. Tao, J.T.S. Irvine, Mater. Res. Bull. 36 (2001) 1245.
[26] L. Gao, J.S. Hong, H. Miyamoto, S.D.D.L. Torre, J. Eur. Ceram. Soc. 20 (2000) 2149.
[27] K.-P. Chen, C. Li, X. Zhang, Y. Huang, Mater. Lett. 57 (2002) 20.
[28] W.-J. Park, W. Jo, D.-Y. Kim, J.-H. Lee, J. Mater. Sci. 40 (14) (2005) 3825.
[29] N. Masahashi, Mater. Sci. Eng. A 452-453 (2007) 721.
[30] J.H. Noh, H.S. Jung, J.K. Lee, J.R. Kim, K.S. Hong, J. Eur. Ceram. Soc. 27 (8-9) (2007) 2937.
[31] R. Licheri, S. Fadda, R. Orrù, G. Cao, V. Buscaglia, J. Eur. Ceram. Soc. 27 (5) (2007) 2245.
[32] T. Takeuchi, Y. Suyama, D. Sinclair, H. Kageyama, J. Mater. Sci. 36 (9) (2001) 2329.
[33] W. Luan, L. Gao, H. Kawaoka, T. Sekino, K. Niihara, Ceram. Inter. 30 (2004) 405.
[34] J. Yang, Z. Wen, Z. Gu, D. Yan, J. Eur. Ceram. Soc. 25 (14) (2005) 3315.
[35] X.J. Chen, K.A. Khor, S.H. Chan, L.G. Yu, Mater. Sci. Eng. A 341 (1-2) (2003) 43.
[36] K.A. Khor, X.J. Chen, S.H. Chan, L.G. Yu, Mater. Sci. Eng. A. 366 (1) (2004) 120.
[37] T. Xu, P. Wang, P. Fang, Y. Kan, L. Chen, J. Vleugels, O. Van der Biest, J. Van Landuyt, J. Eur. Ceram. Soc. 25 (15) (2005) 3437.
[38] M. Okamoto, Y. Akimune, K. Furuya, M. Hatano, M. Yamanaka, M. Uchiyama, Solid State Ionics 176 (7-8) (2005) 675.
[39] U. Anselmi-Tamburini, M.T. Buscaglia, M. Viviani, M. Bassoli, C. Bottino, V. Buscaglia, P. Nanni, Z.A. Munir, J. Eur. Ceram. Soc. 26 (12) (2006) 2313.
[40] S. Brunauer, P.H. Emmett, E. Teller, J. Amer. Chem. Soc. 60 (1938) 309.
[41] T. Roisnel, J. Rodríguez-Carjaval, Physica B 192 (1993) 55 (see also http://www-llb.cea/fullweb/fp2k/fp2k.htm).
[42] T. Roisnel, J. Rodríguez-Carvajal, in: R. Delhez, E.J. Mittenmeijer (Eds.), Proc. of the 7th European Powder Diffraction Conference (EPDIC 7), Trans Tech Publications Ltd., Switzerland, 2000, pp. 118–123, (see also http://www-llb.cea.fr/fullweb/winplotr/winplotr.htm).
[43] L. León-Reina, E.R. Losilla, M. Martínez-Lara, S. Bruque, A. Llobet, D.V. Sheptyakov, M.A.G. Aranda, J. Mater. Chem. 15 (2005) 2489.
[44] J.E.H. Sansom, D. Richings, P.R. Slater, Solid State Ionics 139 (2001) 205.
[45] C.-C. Hwang, T.-Y. Wu, J. Wan, J.-S. Tsai, Mater. Sci. Eng. B 111 (2004) 49.
[46] Y. Xiong, Z.Y. Fu, H. Wang, Y.C. Wang, Q.J. Zhang, Mater. Sci. Eng. B. 123 (2005) 57.
[47] A. Chesnaud, C. Bogicevic, F. Karolak, C. Estournès, G. Dezanneau, Chem. Commun. 15 (2007) 1550.
[48] J.E.H. Sansom, D. Richings, P.R. Slater, Solid State Ionics 139 (2001) 205.
[49] Y. Masubuchi, M. Higuchi, T. Takeda, S. Kikkawa, Solid State Ionics 177 (2006) 263.
[50] H. Okudera, Y. Masubuchi, S. Kikkawa, A. Yoshiasa, Solid State Ionics 176 (2005) 1473.
[51] J.T.S. Irvine, D.C. Sinclair, A.R. West, Adv. Mater. 2 (1990) 132.